Structure
Article

Structure, Assembly, and Mechanism of a PLP-Dependent Dodecameric L-Aspartate β-Decarboxylase

Hui-Ju Chen,[1,2,4] Tzu-Ping Ko,[1,4] Chia-Yin Lee,[3] Nai-Chen Wang,[1,3] and Andrew H.-J. Wang[1,2,*]
[1]Institute of Biological Chemistry, Academia Sinica, Taipei 11529, Taiwan
[2]Institute of Biochemical Sciences
[3]Graduate Institute of Agricultural Chemistry
National Taiwan University, Taipei 10617, Taiwan
[4]These authors contributed equally to this work.
*Correspondence: ahjwang@gate.sinica.edu.tw
DOI 10.1016/j.str.2009.02.013

SUMMARY

The type-I PLP enzyme L-aspartate β-decarboxylase converts aspartate to alanine and CO_2. Similar to the homodimeric aminotransferases, its protein subunit comprises a large and a small domain, of 410 and 120 residues, respectively. The crystal structure reveals a dodecamer made of six identical dimers arranged in a truncated tetrahedron whose assembly involves tetramer and hexamer as intermediates. The additional helical motifs I and II participate in the oligomer formation. Triple mutations of S67R/Y68R/M69R or S67E/Y68E/M69E in motif I produced an inactive dimer. The PLP is bound covalently to Lys315 in the active site, while its phosphate group interacts with a neighboring Tyr134. Removal of the bulky side chain of Arg37, which overhangs the PLP group, improved the substrate affinity. Mutations in flexible regions produced the more active K17A and the completely inactive R487A. The structure also suggests that substrate binding triggers conformational changes essential for catalyzing the reaction.

INTRODUCTION

L-Aspartate β-decarboxylase (ASD; EC 4.1.1.12) catalyzes the conversion of L-aspartic acid into L-alanine and CO_2. Studies of ASD began in the 1950s; it was first discovered by Meister et al. (1951) and later was also shown to have aminotransferase (AT) activity (Novogrodsky et al., 1963). The holoenzyme comprises six dimers of identical subunits. The dodecamer is stable at low pH but dissociates into dimers as the pH increases (Bowers et al., 1970). Each subunit has a molecular weight of about 60 kDa and contains one pyridoxal 5′-phosphate (PLP) as an essential cofactor (Tate and Meister, 1970). The enzyme also catalyzes β-elimination reactions of L-aspartate analogs (Tate and Meister, 1971). For cysteine sulfinate, it even showed a much higher k_{cat} than for aspartate when the substrate was at a saturating concentration (Soda et al., 1964). The presence of various α-keto acids was shown to enhance the ASD activity, probably by regenerating PLP from pyridoxamine 5′-phosphate (PMP), an intermediate of the AT reaction. ASD is about 100 residues larger than AT, with which it has only limited sequence homology, mostly in the PLP-binding domain (Chen et al., 2000). Before the ASD sequence was published, Graber et al. (1999) reported that they could convert AspAT into a β-decarboxylase by site-directed mutagenesis of the putative active-center amino acids. Today, at least a dozen ASD sequences are known, as well as nine other "extraordinarily long" AT sequences (Wang and Lee, 2006). They show 40%–80% identities in the 530–560 amino acids, suggesting a common protein fold.

The PLP enzymes, with their great catalytic versatility, have been classified into several families according to the different protein folds (Jansonius, 1998). Four of them, types I–IV, catalyze transformations of amino acids, including reactions at the α, β, and γ positions (Eliot and Kirsch, 2004). Type I enzyme, to which both ASD and AT belong, contains a PLP-binding domain with a central β strand surrounded by several α helices. The key feature of catalysis by PLP enzymes is the conjugated double bonds of the Schiff base of the substrate amino acid and the pyridoxal ring, facilitating negative charge development at the Cα atom and subsequent cleavage of the bond perpendicular to the plane of the conjugated bond system (Dunathan, 1966).

Some of these enzymes have been exploited in industrial process. For example, ASD in the immobilized *Pseudomonas dacunhae* cells was used to convert L-aspartate to L-alanine (Chibata et al., 1965). Later, this reaction was also used to facilitate separation of D-aspartate from the D,L-mixture produced by reacting fumaric acid with ammonia (Rozzell, 1991). Although D-aspartate is highly demanded in manufacturing many antibiotics, the second product L-alanine can also be used, for example, in making food additives.

Recently, we cloned and expressed the recombinant ASD proteins from *Alcaligenes faecalis* CCRC 11585 and *Pseudomonas* species ATCC 19121 (Chen et al., 2000; Wang and Lee, 2006). Denoted AsdA and AsdP here, each protein has a C-terminal His_6-tag that facilitates efficient purification yet retains the dodecamer integrity and full enzymatic activity. Although crystals of ASD from *Achromobacter* and *Pseudomonas* (Wilson and Kornberg, 1963; Chibata et al., 1967) and the EM-images of the *Pseudomonas* and *Alcaligenes* enzymes

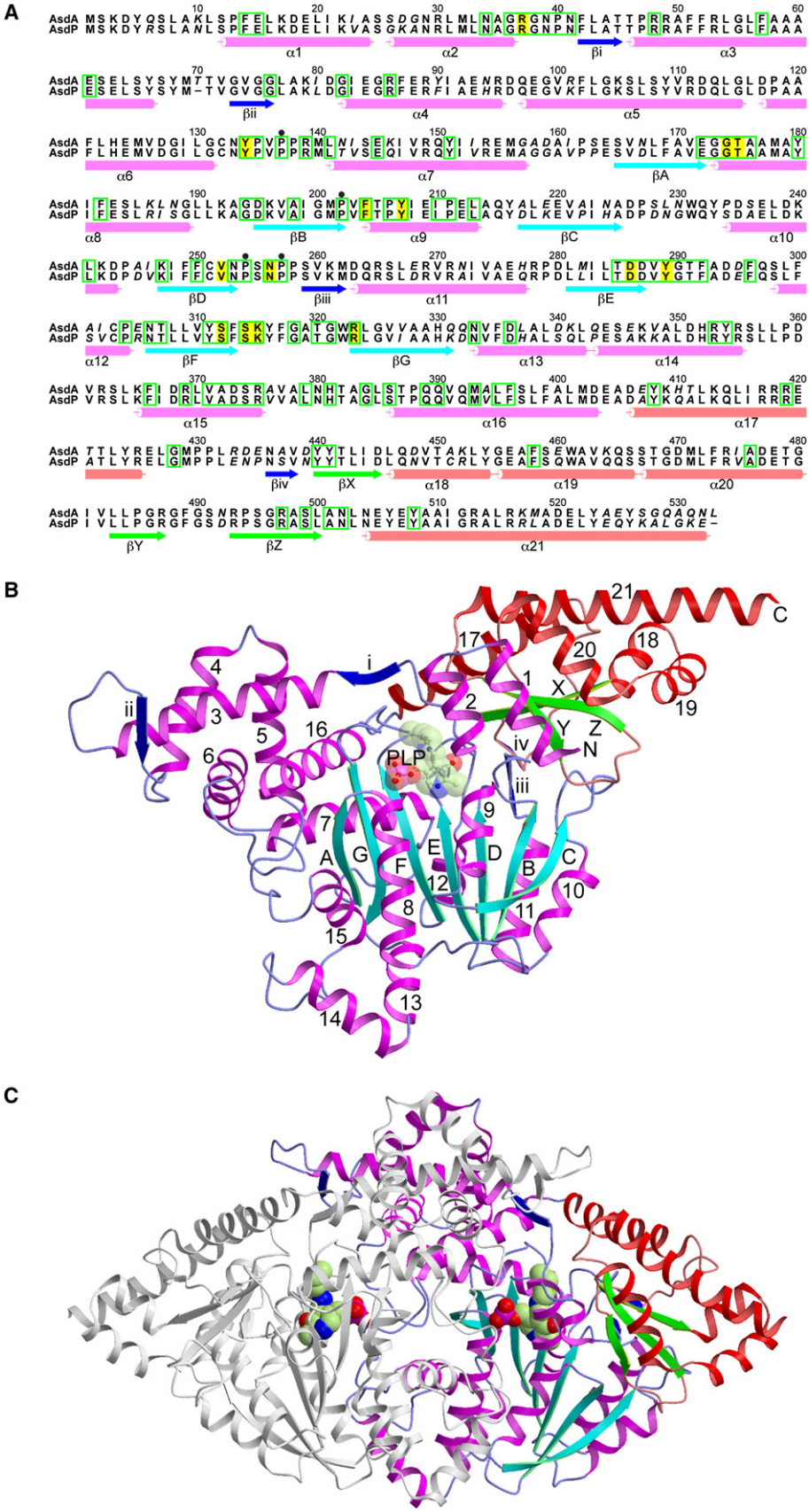
A
AsdA
AsdP
α1
α2
βi
α3
βii
α4
α5
α6
α7
βA
α8
βB
α9
βC
α10
βD
βiii
α11
βE
α12
βF
βG
α13
α14
α15
α16
α17
βiv
βX
α18
α19
α20
βY
βZ
α21
B
C
N
PLP
i
ii
iii
iv
X
Y
Z
A
B
C
D
E
F
G

with the dodecameric character (Bowers et al., 1970; Tate and Meister, 1970) were obtained decades ago, no atomic structure has been available so far. In a previous work, we identified the active-site lysine residue by sequence comparison (Wang and Lee, 2006) and recently also modeled the PLP-binding domain using the AT coordinates as a template (Wang et al., 2008). Here, we determined the three-dimensional atomic structure of this enzyme by use of a multiple anomalous diffraction (MAD) method, which revealed a novel dodecameric assembly with a truncated tetrahedron symmetry. On the basis of the crystal structure, a number of mutants at the subunit interface and active site were designed and characterized to help understand the molecular assembly and catalytic mechanism.

RESULTS AND DISCUSSION

Structure Determination and Comparison

The *Pseudomonas* and *Alcaligenes* enzymes were crystallized in a cubic and an orthorhombic unit cell. Similar dodecamers of AsdP and AsdA are seen in both crystals. The cubic crystal contains one monomer in an asymmetric unit, and the orthorhombic crystal contains six monomers. Details of phasing and refinement are described in Experimental Procedures. Although the initial electron density map of the cubic crystal of AsdP at 5.5 Å resolution only allowed gross fitting of the PLP-binding domain and some surrounding α helices, the crude dodecamer model turned out to be effective in yielding a correct molecular replacement solution for the orthorhombic crystal of AsdA. Subsequently, by exploiting the six-fold noncrystallographic symmetry (NCS) and the data set at a higher resolution of 2.5 Å, a nearly complete protein model was obtained. The model was then placed back into the cubic unit cell and refined as well. The crystals were first grown at pH 8.4 (AsdP) and pH 7.4 (AsdA), whereas later crystallization at pH 5.8 improved the resolution of the orthorhombic crystal of AsdA to 2.0 Å, in which additional electron densities from a small N-terminal helical segment and part of the C-terminal His_6-tag became visible.

The primary sequences of AsdA and AsdP differ in length by two amino acids. Consequently, the residues are numbered according to the longer AsdA sequence (Figure 1A). Thr70 is regarded as a deletion in AsdP. Each of the refined polypeptide models contains a PLP molecule that is covalently bound to the side-chain amino group of Lys315. The refinement statistics are shown in Table 1. The polypeptide chain is folded into two major domains: the large N-terminal PLP-binding domain (L domain, 12–405) and the small C-terminal domain (S domain, 406–532). The central β sheet of the L domain comprises six parallel strands (A–F) and one antiparallel strand (G). Helices α3–α7 and α16 constitute a helical subdomain adjacent to the central β sheet. On the other side, helices α13–α15 also form a cluster. The S domain contains three antiparallel β strands (X, Y, and Z) and five α helices (α17–α21). Two short β strands (iii and iv) run antiparallel at the domain interface (Figure 1B; see Figure S1 available online). The two N-terminal helices α1 and α2 are flexible.

There are four *cis*-proline residues (137, 202, 254, and 257) in each subunit, all strictly conserved among the 12 ASD sequences (Figure 1A; Wang and Lee, 2006). They play important structural roles. In particular, Pro254 and Pro257 are located between strands βD and βiii, forming part of the PLP-binding site. We have shown that the mutant P257H was inactive (Wang et al., 2008), presumably because of the disturbed active-site structure. The glycine-like conformations of Val377 and Met429 account for the 0.4% outlying residues in the Ramachandran plot (Table 1; Laskowski et al., 1993). Although not conserved in the ASD sequences, these two residues are also structurally important.

The root-mean-square deviation (RMSD) between the two AsdA structures at different pH levels is 0.35 Å for 3090 pairs of Cα atoms in the six monomers. The individual polypeptide chains deviate by 0.24–0.38 Å. They differ from the AsdP structure by an overall RMSD of 1.39 Å. If the L and S domains are superimposed separately, the average RMSDs are 0.55 Å and 0.65 Å. There is a slight rotation (about 4°) in the relative disposition of the two domains (Figure S2). Searches with the *DALI* server (Holm and Sander, 1996) for structurally homologous proteins confirmed the kinship of ASD to the AT family of PLP enzymes (or α family), which has the type I fold. AspAT from *Thermus thermophilus* (1BJW) has the highest Z score of 26.0 (RMSD = 2.9 Å). Cystalysin from *Treponema denticola* (1C7N) ranks second (Z = 24.2; RMSD = 3.2 Å) and also catalyzes bond cleavage at the β carbon (Krupka et al., 2000). Both the L and S domains of ASD and AT show some similarity, with an RMSD of about 2.0 Å for 220 and 80 matched Cα pairs (Figure S2). However, ASD contains the additional helical motifs I and II of α3–α7 and α13–α16, which are not seen in any of the AT or other type I structures (Figure S3), and there are also variations in the S domain. The binding site of PLP is located in a cleft between the L and S domains adjacent to another subunit, which forms a dimer (see below). ASD and AT use virtually the same repertoire of enzyme-cofactor interactions, including the salt bridge of the 5′-phosphate and Arg323 (Arg266 in AT), the stabilization of the protonated N4 by Asp286 (Asp222), and several hydrogen bonds, including one between the phosphate and Tyr134 (Tyr70) from the other subunit (Figure S4).

Oligomer Interface

Two identical ASD momomers associate tightly into a dimer (Figure 1C), which is the basic unit in the enzyme assembly

Figure 1. The Monomer and Dimer Structures of ASD

(A) The amino acid sequences of AsdA and AsdP are aligned, with different residues shown in italics. Cylinders and arrows below the sequences indicate α helices and β strands. Residues that interact with the cofactor PLP are shaded in yellow. Those enclosed in green boxes are conserved in twelve known sequences of ASD. The four *cis*-prolines are marked with bullets.

(B) The ASD monomer consists of two domains. The helices and strands in the N-terminal L domain are colored magenta and cyan. Those in the C-terminal S domain are in red and green. They are labeled with numbers and single letters as in (A). The side chain of Lys315 and the covalently bonded PLP are shown as spheres.

(C) The dimer is the basic building unit of ASD. One monomer is colored the same as in (B) and the other in gray. Note the extensive interface between the two monomers.

Table 1. Data Collection and Refinement Statistics of the ASD Crystals

	AsdP + $HgCl_2$ (remote) (edge)		AsdP (pH 8.4)	AsdA (pH 7.4)	AsdA (pH 5.8)	R487A (pH 7.4)
Data collection						
Source	NSRRC BL13B1		NSRRC BL13B1	NSRRC BL17B	PF BL17A	PF BL17A
Wavelength (Å)	0.991	1.010	1.000	1.000	1.000	1.000
Space group	F432		F432	$C222_1$	$C222_1$	$C222_1$
Unit cell *a*, *b*, *c* (Å)	296.8		298.9	149.7	150.0	149.9
	296.8		298.9	216.1	217.1	216.2
	296.8		298.9	208.7	207.2	208.6
Resolution (Å)	30–4.75 (4.92–4.75)		30–3.3 (3.42–3.30)	50–2.5 (2.59–2.50)	30–2.0 (2.07–2.00)	30–2.65 (2.74–2.65)
Number of observations	92705 (9966)	106895 (11137)	189703 (16082)	499995 (44790)	736492 (70534)	164814 (16893)
Unique reflections	6127 (604)	6225 (602)	17608 (1684)	115036 (11108)	224783 (22282)	97136 (9108)
Completeness (%)	99.0 (100.0)	99.2 (99.8)	99.7 (98.7)	98.6 (96.1)	99.7 (100.0)	92.2 (94.8)
Average I / σ(I)	22.6 (3.8)	21.5 (3.4)	23.4 (3.3)	11.2 (2.4)	12.6 (1.6)	11.3 (2.2)
R_{merge} (%)	10.5 (47.6)	10.3 (49.6)	9.9 (59.3)	12.1 (49.2)	6.8 (34.4)	9.4 (44.6)
Refinement						
Number of reflections			16032 (1403)	108127 (9659)	214039 (19102)	85058 (7130)
R_{work} (95% data)			0.228 (0.285)	0.175 (0.241)	0.156 (0.222)	0.175 (0.278)
R_{free} (5% data)			0.293 (0.301)	0.234 (0.317)	0.204 (0.260)	0.238 (0.364)
R.m.s.d bond distance (Å)			0.015	0.011	0.015	0.014
R.m.s.d bond angle (°)			1.9	1.5	1.7	1.8
Ramachandran plot (% residues)						
In most favored regions			80.0	90.6	92.7	89.1
In additional allowed regions			19.6	9.0	6.9	10.0
In generously allowed regions			0.2	0.0	0.0	0.5
In disallowed regions			0.2	0.4	0.4	0.4
Average B ($Å^2$) / No. of non-H atoms						
Protein			77.8 / 4095	38.5 / 24313	24.5 / 24437	38.5 / 24221
Water			70.7 / 50	42.8 / 2207	40.0 / 3290	43.8 / 1912
Ligand (PLP, Cl^-)			61.3 / 15	30.3 / 90	17.2 / 96	27.9 / 90
PDB accession numbers			2ZY2	2ZY3	2ZY4	2ZY5

Numbers in parentheses are for the highest resolution shells. All positive reflections were used in the refinement.

(Bowers et al., 1970). The dimer interface buries an extensive surface area of 3600 $Å^2$, which makes up more than 16% of the 22,000 $Å^2$ molecular surface on each monomer. Specific interactions include more than 30 hydrogen bonds and several clusters of nonpolar side chains. The strands βi and βii from two different monomers are associated in two short antiparallel ribbons at the dimer interface. In addition to the similar protein fold of the monomers, the ASD dimer also bears much resemblance to the functional dimer of AT in terms of the disposition of the L and S domains (Figure S2). The two L domains are back to back, whereas the S domains protrude in opposite directions. The dimers of ASD and AT can be superimposed with an RMSD of about 2.4 Å for 440 Cα atoms, in which the PLP-binding L domains are especially well matched. The dimer interface of AT is also extensive, covering 3000 $Å^2$ on the 18,000 $Å^2$ surface area of each monomer. Participation of the helical motifs I and II in the dimeric assembly accounts for the larger interface of ASD than AT. However, ASD does not function as a dimer as does AT; instead the enzyme activity depends on additional dimer-dimer interactions in a dodecamer.

The dodecamer structure of ASD has a diameter of about 150 Å, with a central cavity measuring 25 Å (Figure 2A). The arrangement of subunits in the dodecamer is best depicted using a truncated tetrahedron (Figure 2B). The molecular dyads of the dimers are aligned exactly along the three orthogonal two-fold axes. There are also four intersecting three-fold axes, each located at the center of the parallel planes of triangle and hexagon (Figure 2C). The formation of a dodecamer buries 4800 $Å^2$ (about 13%) surface areas on each dimer, which is in contact with four neighboring dimers. The interface is contributed by at least 110 residues (55 residues per monomer; Table S1) located in helices α3, α4, α5, α7, α16, α17, and α21. The interactions involve more polar residues than nonpolar, with a ratio of about 7 to 3.

Five mutants of AsdP were designed to probe the interface near the three-fold axis (Figure S5) without disturbing the active site structure and dimer interface. Three had the residues Ser67, Tyr68, and Met69 in a loop all replaced by arginine, glutamate, or alanine. The other two, E84K/E88K and R425A, altered the charged residues. The triple mutants of S67R/Y68R/M69R and S67E/Y68E/M69E were completely inactive, whereas

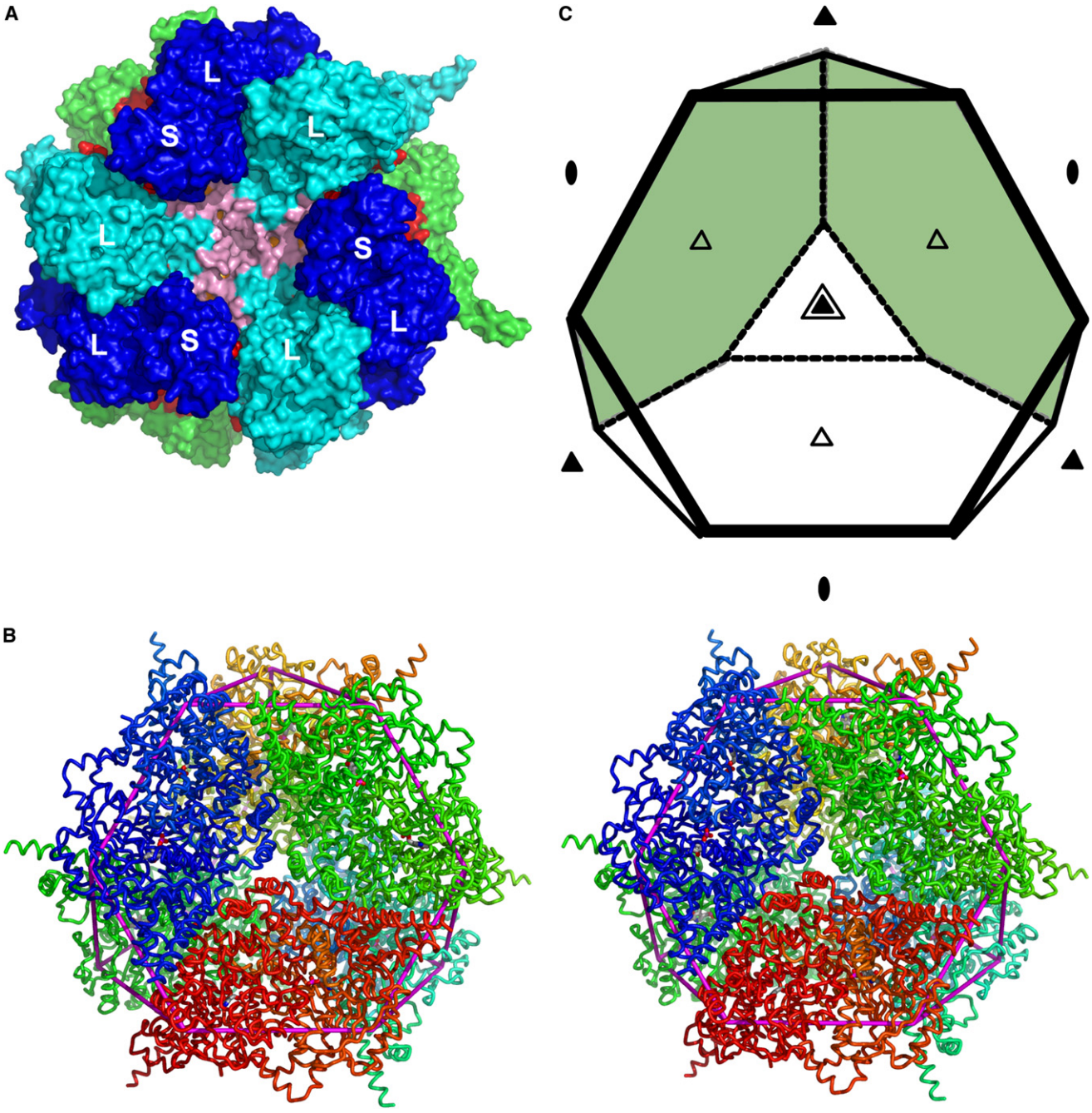

Figure 2. The Quaternary Structure of the Dodecamer

(A) Surface presentation of the dodecamer is viewed along a three-fold axis. Locations of the L and S domains are marked. Some dimers are colored cyan and blue; others are in green and lemon (not seen). One dodecamer interface region from helix α3 to helix α5 is colored pink, and another interface region of helices α7, α16, and α17 is colored red.

(B) Stereo view of the dodecamer is shown as peptide tracing, spectrum-colored in red, green, and blue by chains. A truncated tetrahedral cage enclosing the dodecamer is shown in magenta, as are the PLP molecules.

(C) The four hexagonal and four triangular faces of the dodecamer and the two-fold and three-fold symmetry axes are shown in a schematic diagram.

S67A/Y68A/M69A retained less than 1% activity. The double mutant E84K/E88K had 13% activity, and R425A had 2.5% activity (Figure 3A). Similar circular dichroism (CD) spectra to that of the wild type excluded major structural adversity caused by these mutations (Figure S6). UV/Vis absorption spectra of the mutants also showed the peak at 360–370 nm characteristic of bound PLP (Figure S7). Further analysis by gel filtration at pH 5 showed that some mutants prevented the dodecamer assembly (Figure 3B). The correlation between the assembly and activity is manifested in the existence of the inactive mutants

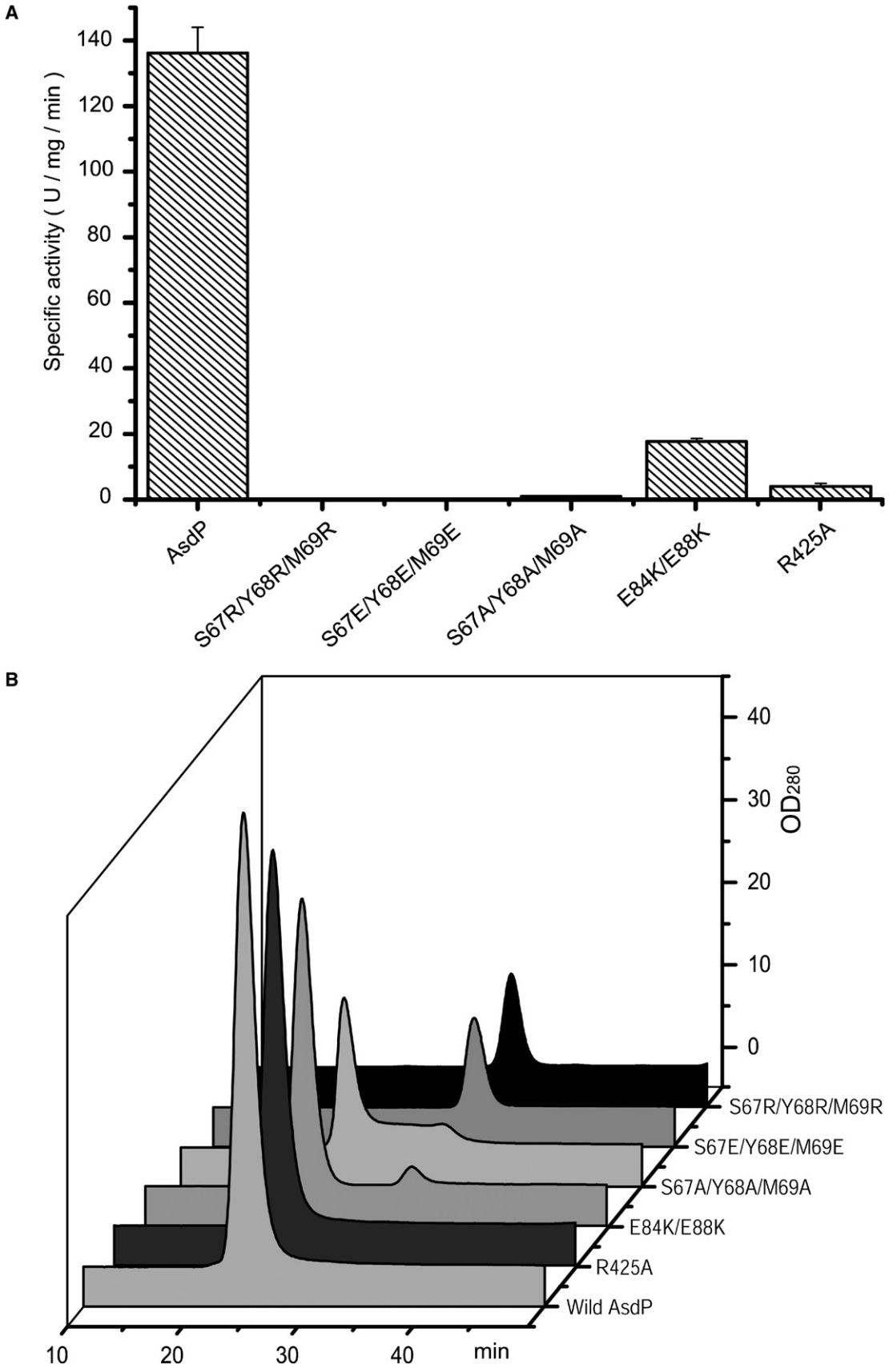
A
Specific activity (U / mg / min)
140
120
100
80
60
40
20
0
AsdP
S67R/Y68R/M69R
S67E/Y68E/M69E
S67A/Y68A/M69A
E84K/E88K
R425A
B
40
30
20
10
0
OD280
S67R/Y68R/M69R
S67E/Y68E/M69E
S67A/Y68A/M69A
E84K/E88K
R425A
Wild AsdP
10
20
30
40
min

S67R/Y68R/M69R and S67E/Y68E/M69E exclusively as a dimer. Similar correlation is seen in the other mutants, suggesting that the pH effect on the ASD activity is not only a result of the higher concentration of proton as a reactant, but also depends on a properly organized dodecamer structure. The crystal structure of AsdP at pH 8.0 in fact shows a looser packaging of the subunits than that of AsdA at pH 7.4, which, in turn, is looser than that of AsdA at pH 5.8 (Figure S5). The AsdP mutants S67A/Y68A/M69A and E84K/E88K also tended to dissociate into dimers, but R425A remained as an intact dodecamer (Figure 3). The lower activity of R425A than E84K/E88K may be caused by lack of some important polar interactions at the three-fold interface.

Dodecamer Assembly

For the assembly of a functional dodecamer, the dimers are exchangeable between the enzymes from different species (Tate and Meister, 1970). To investigate the aggregation states in solution and to seek possible assembly pathways, we used analytical ultracentrifuge (AUC) under various solvent conditions. In Figure 4A, the 5.9S and 19.6S particles corresponding to the dimer and dodecamer are similar to those observed previously (Bowers et al., 1970). The calculated masses of about 120 kDa and 730 kDa correlate very well with the actual molecular weights (Figure 4B). As the pH varies from 5 to 9, the equilibrium shifts from all-dodecamer to all-dimer. However, there are two minor peaks that possibly represent two different intermediates, most prominent at pH 8.0 (Figure 4C). Because sedimentation rate depends on molecular shape, a different friction coefficient was used in calculating the corresponding masses. They turned out to be about 230 kDa (tetramer) and 390 kDa (hexamer), each constituting up to 10% of the total protein (Figure 4C). Experiments at pH 7 also showed that high ionic strength favors dissociation of the dodecamer (Figure 4D), consistent with the mostly polar nature of the dimer-dimer interface. The individual contact surface areas between dimers are relatively small (about 1200 $Å^2$), but collectively they are extensive (4800 $Å^2$ per dimer). The lack of significant intermediates between the dimer and dodecamer, especially at low pH, indicates that the assembly process is highly cooperative. Two adjacent dimers, with perpendicular dyads, are associated into a tetramer. Two possible hexamers, one bowl-shaped, another plane-shaped (Figure 4E), can be put directly together to form a dodecamer, or each can associate with a tetramer and another dimer.

A few other dodecameric enzymes also assemble with the tetrahedral 23 point-group symmetry as seen in ASD: a tetrahedral aminopeptidase with a binuclear zinc active center (TET; Russo and Baumann, 2004), a catabolic ornithine transcarbamoylase (OTC; Villeret et al., 1995), and a peptidyl cysteine decarboxylase (EpiD; Blaesse et al., 2000), which also catalyze transformation of amino acids; an antioxidant protein that binds and protects DNA (Dps; Grant et al., 1998); and a cyclomaltodextrinase (CDase; Lee et al., 2002). The basic units of these enzymes are dimers (TET, Dps, and CDase) or trimers (OTC and EpiD), but all function as a dodecamer. TET was also found to assemble into an octahedral quaternary structure with a large central cavity (Schoehn et al., 2006). The Dps is related to the 24-subunit ferritin with 432 symmetry but efficiently uses H_2O_2 to oxidize Fe(II) to Fe(III). The dodecameric structures of OTC, EpiD, and CDase are all implicated in regulating substrate binding and/or access to cofactor.

Substrate Binding Mechanism

As mentioned above, the active site configuration of ASD is similar to that of AT (Figure S4), but there are several differences. One is the presence of Arg37, whose outstanding side chain occupies the substrate-binding space and tends to stack with the PLP ring (Figure 5A). Others include the surrounding Tyr207, Tyr440, and Tyr441, which are suspected to participate in the reaction, perhaps by providing protons. On the basis of these observations, three mutants—R37A, Y207F, and Y441F—were produced. Tyr134 of ASD is equivalent to Tyr70 of AT, which binds to the PLP across the dimer interface (Figure S4). In ASD, it is also hydrogen bonded to the Schiff base of Lys315-PLP and may be implicated in proton transfer. On the other hand, unlike the more open ones of AT and other enzymes, the active sites of ASD are deeply buried (Figure 5B). Interestingly, a positively charged patch contributed by Lys17 and Arg487 emerges on the surface where the substrate molecule must penetrate to reach the active site (Figures 5C and 5D). Therefore, we made three other mutants—Y134F, K17A, and R487A—plus an additional mutant, K315A. All the AsdA mutants produced similar CD spectra as the wild type (Figure S6) and retained significant activity, except R487A, which was completely inactivated (Table 2). The reaction velocity versus substrate concentration curves appeared sigmoidal especially for some mutants (Figure S8), indicating substrate-binding cooperativity. At neutral pH (7.4), prominent sigmoidal curves were also observed for the wild-type AsdA (data not shown). Because the dodecameric enzyme tends to dissociate into dimers at higher pH, presumably the cooperativity is a result of subunit interactions (discussed in the next section).

The k_{cat} values of the mutants K17A and R37A were 30% and 40% lower than that of the wild type, but their $K_{0.5}$ values were decreased by about 50%, resulting in higher overall activity, especially in K17A. Lys17 is located in a flexible N-terminal region, as reflected by its B value (Figure S9), and its side chain is likely to shift aside to allow entrance of the substrate to the active site. Removal of the bulky side chain of Arg37, despite its positively charged nature, also facilitated the binding of substrate molecule. A higher $K_{0.5}$ value and a lower k_{cat} value of Y134F suggested additional roles of Tyr134 in catalysis besides binding to PLP across the dimer interface. The mutation also affected the dodecamer assembly (Table 2). Although Y441F also caused its partial dissociation into dimers, Y207F had moderate effects on the enzyme. These results indicated that the hydroxyl groups of Tyr207 and Tyr441 are not essential to the catalytic reaction. Interestingly, removal of the side chain of Lys315 did not completely

Figure 3. Effects of Mutation on Activity and Assembly of AsdP

(A) Specific activity of the AsdP mutants is compared with the wild-type enzyme. All mutants were inactivated except E84K/E88K, which retained 1/8 of activity. (B) Gel filtration analysis of the mutants showed that the dodecamer assembly was impaired. The absorbance at 280 nm (OD_{280}) was measured in milli-absorbance units (mAU). Both experiments were carried out at pH 5.0.

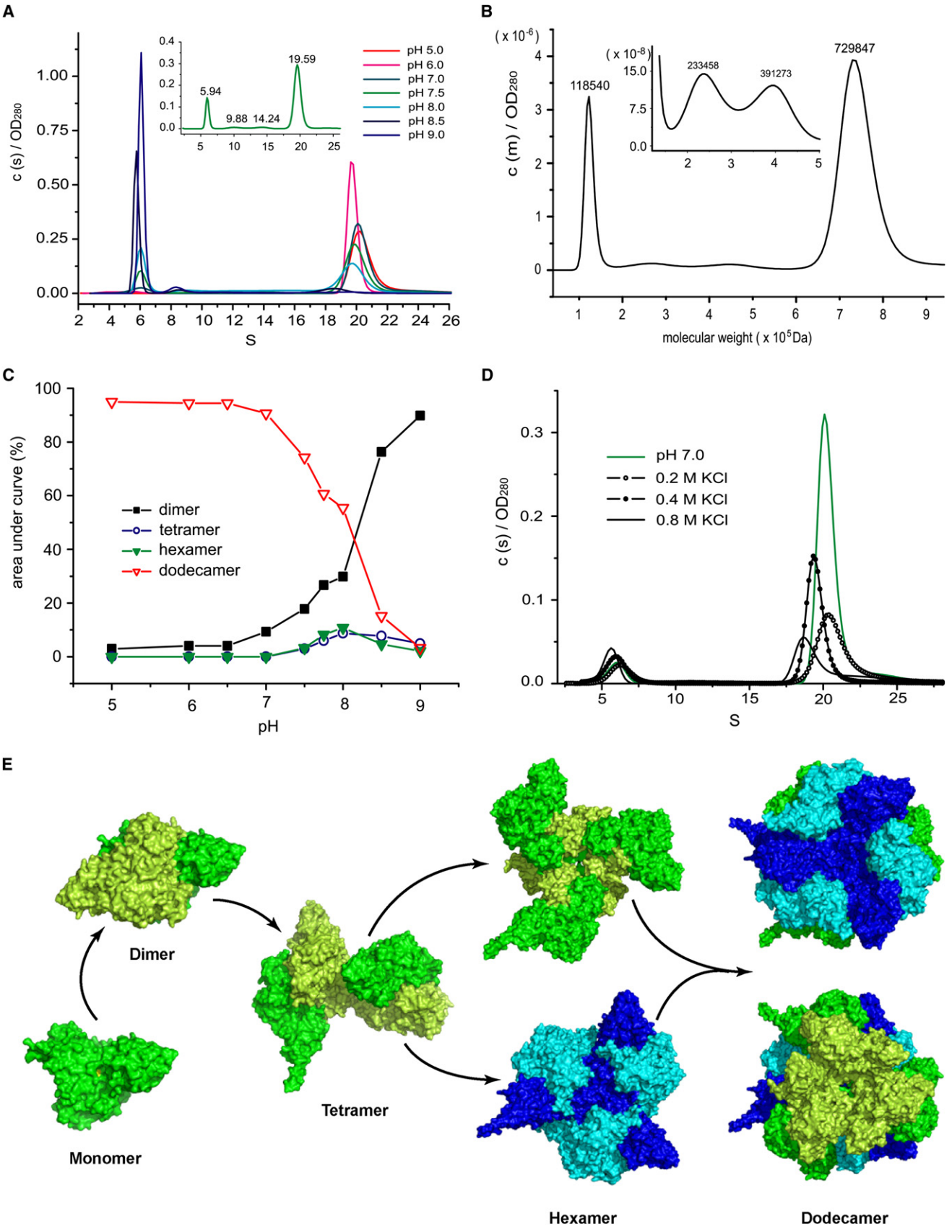
A
c (s) / OD280
S
pH 5.0
pH 6.0
pH 7.0
pH 7.5
pH 8.0
pH 8.5
pH 9.0
5.94
9.88
14.24
19.59
B
(x 10-6)
c (m) / OD280
molecular weight (x 10^5 Da)
118540
233458
391273
729847
C
area under curve (%)
pH
dimer
tetramer
hexamer
dodecamer
D
c (s) / OD280
S
pH 7.0
0.2 M KCl
0.4 M KCl
0.8 M KCl
E
Dimer
Monomer
Tetramer
Hexamer
Dodecamer

inactivate the enzyme. Instead, it reduced the substrate affinity. In AT, an equivalent mutant of K258A also remained active (Toney and Krisch, 1993), but the mechanism was through reduced k_{cat} and K_M, known as Circe effect. In ASD, it seems more likely for Lys315 to be involved in binding PLP than in catalysis. This is supported by UV/Vis spectra, in which K315A did not show the characteristic peak at 370 nm for aldimine PLP, as observed in the wild type and all other mutants (Figure S7).

In AT and other type I PLP enzymes, a conserved arginine residue (Arg497 in ASD, Arg386 in AT, and Arg369 in cystalysin) is responsible for holding the α-carboxyl group of the bound substrate (Figure S10). Significant conformational changes must occur for the side chain of Arg497 to reach the position for substrate binding. In an AT dimer, Arg292 from the other subunit binds to the side-chain carboxyl group of the substrate. The equivalent is not found in ASD and cystalysin, which catalyze reactions at the β carbon. To bind its substrate properly, a second arginine seems not to be necessary for ASD. The inactive mutant of R487A is not related to this kind of interaction. Arg487 is located in the βY-βZ loop and has great flexibility in the structure (Figure S9). Removal of its side chain is unlikely to cause any large disturbance to the overall structure or the dodecamer assembly (Table 2). Indeed, the mutant R487A can be crystallized in an isomorphous unit cell, and its structure can be refined as was the wild type (Table 1). Another possibility is that Arg487 constitutes a second substrate-binding site by presenting a highly positively charged surface adjacent to the active-site cavity, but paradoxically, the companion mutant K17A has an increased activity. The role played by Arg487 and the associated flexible loop is not entirely clear, and it is further obscured by the fact that Arg487 is not conserved in ASD sequences (Figure 1A; Wang and Lee, 2006), although the two flanking glycines are seen in many sequences.

Activity Modulated by Enzyme Conformational Change

Domain movements have been implicated in many enzymes for proper interactions with the substrate molecule(s) that facilitate catalysis. A typical example is seen in AspAT (McPhalen et al., 1992), where two arginine residues, Arg292 and Arg386, each from a different subunit in a dimer, bind to the two carboxylate groups of aspartate, glutamate, oxaloacetate, or α-ketoglutarate and induce the conformational change that rotates the S domain toward the active site, known as domain closure. The active-site configuration then provides an optimized environment for the substrate to form a Schiff base with the cofactor PLP and, for the key residue Lys258, to transfer the proton between the Cα of the substrate and the C4′ of PLP and to usher in a water molecule to produce α-keto acid and PMP. For substrates with different characters like aspartate and phenylalanine, the interactions are variable (Jansonius, 1998). Phenylalanine does not have the negatively charged group to form salt bridge with Arg292 and instead acts by exclusion of solvent molecules from the active-site cavity. For ASD, there seems to be no positively charged residue in the active site to bind to the β-carboxylate group of the substrate, consistent with the lack of strict substrate specificity (Tate and Meister, 1971). In the current crystal structures, both AsdA and AsdP are in an open conformation, compared with AT (Figure S2). Although it may involve Arg497 and the associated loop, the precise mechanism by which substrate binding triggers conformational changes in ASD to facilitate catalysis remains to be elucidated.

According to proposed catalytic mechanisms (Tate and Meister, 1969; Rosenberg and O'Leary, 1985; Brzovic et al., 1990), the reaction of ASD starts with displacing the internal aldimine of Lys315-PLP by the substrate, forming an external aldimine. The free amino group of Lys315 subtracts the α-proton from the substrate, followed by elimination at the β-carbon (Figure S10). In the two-base mechanism of Chang et al. (1982), another base is needed to transfer the β-proton to the intermediate, producing a methyl group. The identity of this second base is uncertain. It can be a surrounding tyrosine (Tyr134), some other amino acid side chain, or a solvent molecule. The α-proton is then retrieved from Lys315, the product alanine is released, and the internal aldimine is regenerated (Figure S10). During the catalysis, polarization by the Schiff base nitrogen or some active-site environment facilitates cleavage of the Cβ-Cγ bond, which presumably is oriented perpendicular to the plane of the conjugated bond system (Dunathan, 1966). The positively charged active-site cavity can provide a driving force for such polarization (Figure S11). It also stabilizes the partially developed negative charge in the intermediate before protonation of the β-carbon.

Because the ASD structures presented here do not contain any bound substrate molecule or analog, their conformation may deviate somewhat from that of an enzyme-substrate complex. For example, the Schiff base of the Lys-PLP is not properly oriented; the N4′ does not form a hydrogen bond with the O3′; rotation of the 5′-phosphate group moves the ring inward, away from the solvent (see Figure 5A); and the entire residue of Arg497 is too far from the PLP to make proper salt bridge with the incoming substrate, even with its side chain rotated and extended in that direction (Figure S10). Movement of the S domain about the L domain as in the domain closure of AT must somehow occur in ASD during the catalysis. But the ASD also has to form a proper dodecamer to be fully active. At each dimer-dimer interface, one dimer contributes 15 residues in the L domain of one monomer and 10 residues in the S domain of the other monomer, and the other dimer has 32 residues involved, all from one L domain (Table S1).

Figure 4. The pH Dependence of the Dodecamer Assembly of AsdA

(A) The distribution of molecular size under various pH conditions was assessed using AUC. Parameters used in calculating the sedimentation coefficients are viscosity = 0.01048 and density = 1.01029.

(B) The curve at pH 7.5 was converted to represent mass distribution. The corresponding masses of dimer and dodecamer were calculated using frictional coefficients f = 1.32–1.35, and those of the intermediates (inset; probably tetramer and hexamer) using f = 1.21–1.25.

(C) Areas under the curves in (A) were integrated to show different proportions of oligomers in various pH conditions. The ratio of dimer: intermediates: dodecamer was roughly 1:1:2 at pH 8.

(D) Under higher ionic strength of KCl, more dodecamers were dissociated into dimers at pH 7.

(E) The proposed assembly mechanism of ASD starts from monomer to dimer, followed by tetramer and two kinds of hexamer. Finally the two hexamers dock together, face to face, to form the spherical dodecamer.

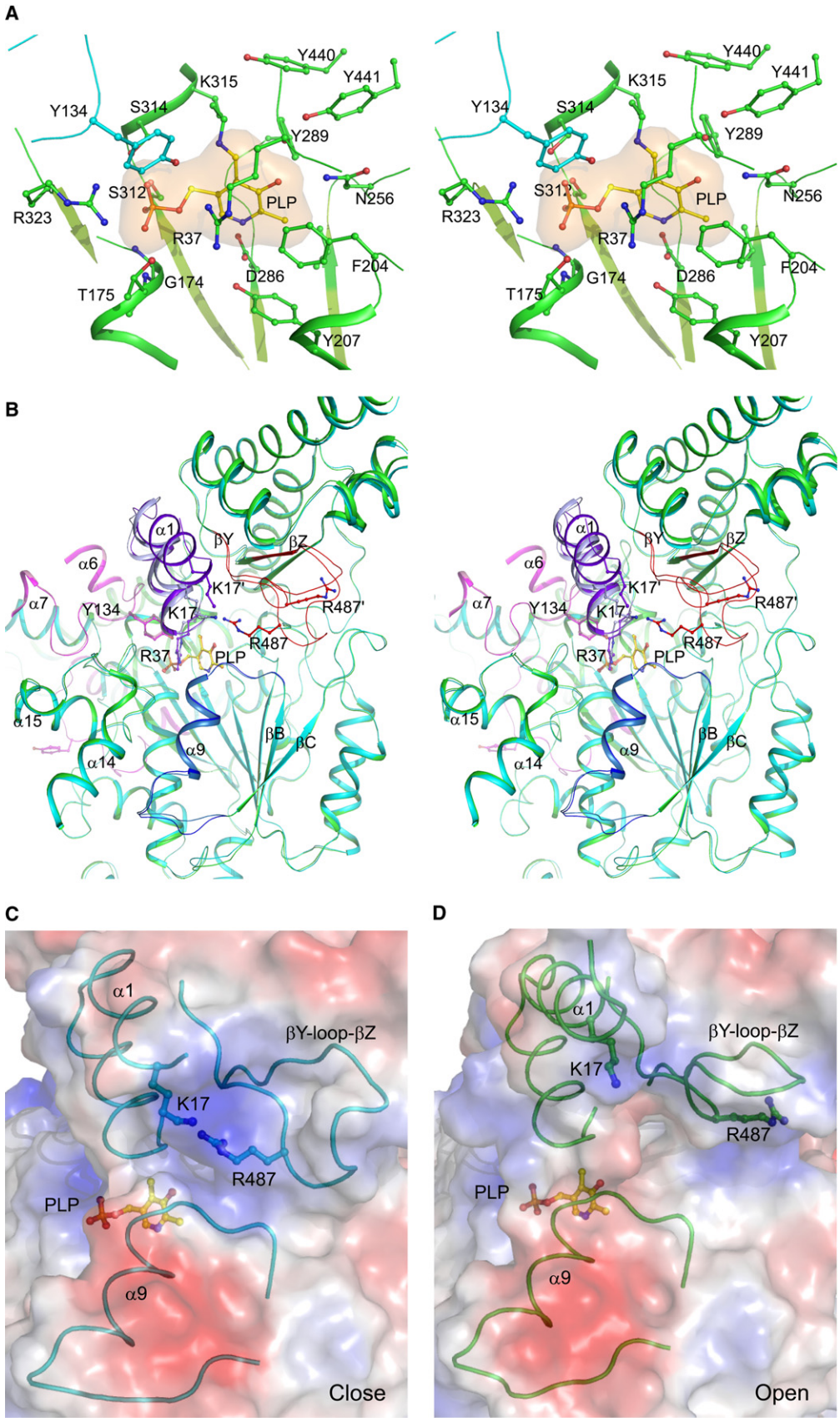
A
Y440
Y441
K315
Y134
S314
Y289
S312
PLP
N256
R323
R37
F204
T175
G174
D286
Y207
B
α1
βY
βZ
α6
K17'
α7
Y134
K17
R487'
R487
R37
PLP
α15
βB
βC
α9
α14
C
α1
βY-loop-βZ
K17
R487
PLP
α9
Close
D
α1
βY-loop-βZ
K17
R487
PLP
α9
Open

Table 2. Effects of Mutations on the Kinetic Parameters of AsdA

AsdA[a]	$K_{0.5}$ (mM)	Hill (h)	V_{max} (mM min^{-1})	k_{cat} (s^{-1})	k_{cat} / $K_{0.5}$ (s^{-1} mM^{-1})	Relative activity (%)	Dimer[b](%)
Wild Type	8.91 ± 0.57	1.18	11.14 ± 0.48	442	49.7	100.0	2.4
K17A	4.77 ± 0.35	1.19	7.83 ± 0.23	311	65.2	131.2	24.4
R37A	5.03 ± 0.54	1.57	6.79 ± 0.16	270	53.6	107.9	10.4
Y134F	13.98 ± 2.63	2.00	6.54 ± 0.31	259	18.6	37.4	40.3
Y207F	9.97 ± 1.20	1.53	7.41 ± 0.24	294	29.5	59.4	10.7
K315A	13.72 ± 3.13	2.09	7.03 ± 0.21	279	20.3	40.9	36.7
Y441F	7.58 ± 1.30	1.71	6.89 ± 0.43	273	36.1	72.7	40.8
R487A	ND[c]	ND	ND	ND	ND	ND	4.1

[a] The conditions of assay are described in Experimental Procedures. V_{max} and $K_{0.5}$ were obtained by using the GraphPad program (Figure S8). The $K_{0.5}$ is half of the substrate concentration for maximal velocity, by sigmoidal model fitting (Hill number (h) $\neq$ 1, calculated using the formula $Y = (V_{max} \times X^h) / (K_{0.5} + X^h)$, where X is substrate concentration and Y is reaction velocity). All data are the average of triplicate repeats. Values of $K_{0.5}$ and V_{max} are expressed as mean ± standard deviation.
[b] The percentage of dimer was determined by analytical ultracentrifugation at pH 6 as described in Experimental Procedures.
[c] ND, activity not detected.

Movement in one subunit will certainly affect the disposition of the others, most likely to trigger conformational changes in a concerted manner. It will, in turn, alter the configuration of each active site and result in different affinity to the substrate. These cooperative events are yet to be elucidated by studying substrate binding to the dodecameric holoenzyme.

CONCLUSION

Despite the poor initial MAD phasing, effective only to 5.5 Å resolution, the homology of the PLP-binding domain of ASD to AT and the presence of six-fold NCS eventually allowed unraveling of the dodecameric structure. Although the holoenzyme assembly is pH dependent, high protein concentration can shift the equilibrium from dimer to dodecamer according to the law of mass action. Because of this, the dodecamer was seen in crystal even at pH 8.4. The dodecamer interface was disrupted by triple mutations at the three-fold axis, and the enzyme existed solely as dimers in solution—inactivated—attesting that the dodecameric structure is essential to the enzyme's function. The useful C-terminal His-tag in protein purification turned out to be very well exposed to the bulk solvent. In fact, a few of the histidines were observed as an extension of the already long helix α21. The spherical dodecameric structure allows different proteins or peptides to be fused with the ASD to create a multivalent assembly for various applications, such as antibody production (Domingo et al., 2001). The interesting results of the mutant K17A with higher overall activity may find potential industrial use. For industry, another goal of engineering is to reduce the side reaction, because prolonged incubation with substrate would result in formation of inactive PMP enzyme (Figure S12). Much remains to be learnt about this dual functional enzyme. Our crystal structures nevertheless open the way for elucidating its mechanism, and encourage further investigation.

EXPERIMENTAL PROCEDURES

Protein Crystallization and Data Collection

Production of the AsdA and AsdP proteins, each containing a C-terminal His_6-tag, followed protocols similar to those described elsewhere (Chen et al., 2000; Wang and Lee, 2006). The vector and host for gene expression were the plasmid of pET-21 and the competent cell of *Escherichia coli* BL21(DE3)pLysS (Novagen). The proteins were purified in two steps: Ni-NTA column and gel filtration. Using imidazole gradient in the 0.1 M Tris-HCl buffer (pH 8.0) containing 0.3 M NaCl, the ASD protein was eluted at about 240 mM. After stabilization by adding 0.1 mM PLP, the enzyme was concentrated using *Amicon* filter (cutoff size, 10 kDa) and further purified by an HPLC gel filtration column (WATERS *k806*). Before crystallization, imidazole was removed by dialysis, the pH was adjusted to 7.5 for AsdA, and the buffer system was replaced by 50 mM HEPES (pH 8.0) for AsdP, both containing a lower NaCl concentration of 0.15 M.

Crystals of AsdA were obtained by mixing equal volumes of the protein solution (35 mg/ml) and a reservoir of 15% PEG4000 and 0.1 M Li-sulfate in 0.1 M Tris-HCl buffer (pH 7.4–8.5) in a hanging drop, and equilibrating at 4°C with the reservoir for a minimum of 3 months. For AsdP (45 mg/ml), sitting drop technique at room temperature was employed, with a reservoir of 40% PEG400 and 0.1 M Li-sulfate in 0.1 M Tris-HCl buffer (pH 8.4). Crystals appeared in about 3 weeks. To obtain better crystals, variation of the pH was carried out using *Additive Screen* (Hampton Research), and higher diffraction resolution (2.0 Å) was achieved for AsdA using 0.2 M imidazole (pH 5.8).

The data of native AsdP crystal and its Hg-derivative were collected at the National Synchrotron Radiation Center (NSRRC) of Taiwan, and so was the data of AsdA crystal at pH 7.4. Data of the AsdA mutant and the low-pH crystal were collected at the Photon Factory (PF) in Japan. All were carried out at cryogenic temperatures. To the mother liquor of the AsdA crystals, 15% glycerol was included as a cryoprotectant. The AsdP crystals were frozen

Figure 5. The Active Site Structure

(A) Stereoscopic view of the PLP binding site shows the surroundings of the bound cofactor (yellow). The phosphate group and the protonated nitrogen are salt-bridged to Arg323 and Asp286. The cyan Tyr134 is from another monomer.
(B) The active-site regions of two different subunits are superimposed. The L and S domains are colored cyan and green. N-terminal helix α1, and loops α6-α7 and βY-βZ, which contain Lys17, Tyr134, and Arg487, respectively, and the covering helix α9 are highlighted in purple, pink, red, and blue. Primed residue numbers are for the more open molecule.
(C) Surface presentation of the closed active site. Positive and negative charge potentials are indicated by blue and red colors. The loops and helices forming the active-site entrance are also shown.
(D) Surface of the more open active site. Intrinsic flexibility of domains, secondary structure elements, and loops should have caused the structural difference.

directly. The heavy atom derivative was prepared by adding 1 mM $HgCl_2$ to a sitting drop that contained the AsdP crystals, followed by soaking for 1 week at 4°C. X-ray fluorescence scanning showed no significant absorption peak, but a steep edge at 1.010 Å. All data were processed using the software package of *HKL2000* (Otwinowski and Minor, 1997), and the statistics are summarized in Table 1.

MAD Phasing and Structure Determination

The two-wavelength MAD data sets containing anomalous signals were analyzed by *SOLVE* (Terwilliger and Berendzen, 1999). Two major mercury sites were located. The phasing was effective only to 5.5 Å resolution, with an overall FOM of 0.23 and a Z-score of 13.2. The electron density map calculated after density modification by *RESOLVE* (Terwilliger, 2000; 2002) showed one monomer in an asymmetric unit, and a large void beyond the molecular boundary, reflecting the high solvent content of 70%. The map featured a central β sheet as a thick plate-like structure, which was surrounded by many α helices as rods of various lengths. A model of the PLP binding domain previously constructed according to the homology with AT (Wang et al., 2008) was fitted manually into the map, using the program *O* (Jones et al., 1991). The placement consistently brought Cys303 near one mercury site. (The second site was later shown to associate with Cys132.) Several α helices with arbitrary sequences were also fitted into the remaining rod-like densities. This model gave an R-value of 0.56 for all native data at 3.3 Å resolution.

A dodecameric model was generated by symmetry operations of the AsdP crystal and then used in search for a molecular replacement solution of the AsdA crystal. When a correct solution was obtained using the program *CNS* (Brunger et al., 1998), the model was reduced to 6 monomers that constitute an asymmetric unit, which yielded an R-value of 0.53 at 3.0 Å resolution. Subsequent refinements employed data sets in which 5% reflections were set aside for R_{free} calculation (Brunger, 1993). With strong NCS restraints, the model was refined to R/R_{free} values of 0.44/0.51 for all data at 2.5 Å resolution. The map quality was improved after six-fold NCS averaging and solvent flattening by *CNS*. The Hendrickson-Lattman coefficients were calculated and used in further density modification and automatic model building by *RESOLVE*. Approximately two-thirds of the amino acid residues were built with correct sequence, and these allowed manual reconstruction of a virtually complete model by cross-reference of the independent protomers. The resulting R/R_{free} were 0.30/0.35, prior to addition of solvent molecules.

The model from the AsdA crystal was fitted back into the original AsdP unit cell by the least-squares procedure of the program *O*. The R-value was 0.35 and the electron density map clearly indicated the deletion of Thr70. The correct amino acid sequence of AsdP was then incorporated.

The 2.0 Å data set of AsdA collected at pH 5.8 could be scaled to the previous 2.5 Å data collected at pH 7.4, but with a high R-value of 0.209, indicating their limited isomorphism. The high-pH model gave an R-value of 0.48 for the low-pH data, which was reduced to 0.28 after rigid-body refinement. Extensions in the N- and C-terminal regions were seen, as well as some conformational changes in the loops, particularly the one containing Arg487. Six chloride ions, each bound to the side chains of Arg49 and Arg53, were included in the solvent model. They corresponded to strong electron densities of 7 σ. The crystal of the mutant R487A turned out to be very similar to the first crystal, both grown at pH 7.4, but it clearly showed the absence of the side chain of Arg487.

The programs *Alscript* (Barton, 1993), *MolScript* (Kraulis, 1991), *Raster3D* (Merritt and Murphy, 1994), and *PyMOL* (DeLano Scientific LLC) were employed to make figures based on the pH 5.8 AsdA model, if not specified otherwise.

Mutagenesis of ASD

Production of the mutants of AsdP and AsdA employed the *QuickChange* site-directed mutagenesis kit (Stratagene). The products were proliferated in *E. coli* XL1-Blue supercompetent cells, and selected clones were verified by sequencing. The selected clones were transformed into *E. coli* BL21(DE3)-pLysS for protein expression. All mutants were checked using CD spectroscopy. The spectra from 190 nm to 250 nm in 0.1 nm steps were recorded using a Jasco *J-715* (Rev.1.00) CD spectrophotometer (Tokyo, Japan) in 1 mm path-length cell and averaged over three scans. These turned out to be virtually identical to those of the wild-type enzymes.

Measurement of Enzyme Activity

Measurement of the decarboxylation activity of AsdP and its mutants followed the previous protocols (Wang and Lee, 2006, 2007). The assays were carried out at pH 5.0 and 37°C. After stopping the reaction by boiling, the products were derivatized with o-phthaldialdehyde (OPA) reagent and analyzed by HPLC. The mutant proteins of AsdP (0.2 mg/ml) were also analyzed by gel filtration chromatography at pH 5.0 with a *Sephadex* 200HR column (10/30; GE Healthcare).

The kinetic parameters of AsdA and its mutants were calculated on the basis of the reaction velocity at different substrate concentrations. Measurement of the activity was carried out using 200 μl solutions containing 5 μg protein in 100 mM Na-phosphate buffer (pH 5.0), 150 mM NaCl, and 20 μM PLP incubated at 25°C for 30 min. The reactions were started by addition of various concentration of L-aspartate and then stopped by 1/10 volume of 1 N NaOH after 1 min. The reaction products were then derivatized with OPA and analyzed using an HPLC ZORBAX Eclipse AAA column (4.6 × 150 mm, 5 μm, Agilent) equilibrated with 20 mM Na-phosphate buffer (pH 7.8). A 0%–60% linear gradient of acetonitrile/methanol/water mixture (45:45:10) was used in elution, and the profile monitored by a fluorescent detector (1100 FLD; Ex 340nm, Em 460 nm).

Determination of Molecular Size by AUC

Sedimentation velocity experiments were conducted at 20°C with a Beckman Optima XL-I AUC equipped with absorbance optics. The AsdA samples were diluted to final concentrations of 0.4 mg/ml using 0.1 M Tris-HCl buffer and 0.15 M NaCl with appropriate pH value 6–12 h prior to analysis. Standard 12-mm aluminum double-sector centerpieces were filled with the protein solution, whereas the blank buffer was used in the reference cell. Before each run, cells were thermally equilibrated for at least 1 h in a 4-hole (AnTi60) rotor of the instrument. Quartz windows were used with absorbance optics (OD_{280nm}) in a continuous mode without averaging. No time interval was set between scans. Rotor speed was 40,000 rpm. Data were analyzed with a *c(s)* distribution of the Lamm equation solutions calculated by the program *SEDFIT* (www.analyticalultracentrifugation.com) assuming the regularization parameter *p* to be 0.95 (high confidence level). The weighted average sedimentation coefficient (*S*) was obtained by integration over the range of each peak. All *S* values were corrected for the viscosity and density of water at 20°C. The areas under the curve of *c(s)* were integrated using the program *Origin* 7.0 (Edwards, 2002).

ACCESSION NUMBERS

Coordinates and structure factors for the crystal of AsdP, and the wild-type high-pH and low-pH, and the R487A mutant crystals of AsdA have been deposited in the PDB with accession codes 2ZY2, 2ZY3, 2ZY4, and 2ZY5, respectively.

SUPPLEMENTAL DATA

Supplemental data include one table and twelve figures and can be found with this article online at http://www.cell.com/structure/supplemental/S0969-2126(09)00095-1.

ACKNOWLEDGMENTS

We thank National Synchrotron Radiation Research Center of Taiwan, Photon Factory of Japan, and Advanced Light Source of UC Berkeley for beam time allocations. We also thank Shu-Chuan Jao and Hui-Chuan Chang for their advice in the ITC and AUC experiments. This work was supported by grants from the National Science Council of Taiwan, ROC (NSC94-2313-B-002-049 and NSC95-2811-B-002-055 to C.Y.L. and NSC-95-3112-B-011-015-Y to A.H.J.W.).

Received: October 23, 2008
Revised: February 5, 2009
Accepted: February 18, 2009
Published: April 14, 2009

REFERENCES

Barton, G.J. (1993). ALSCRIPT: a tool to format multiple sequence alignments. Protein Eng. *6*, 37–40.

Blaesse, M., Kupke, T., Huber, R., and Steinbacher, S. (2000). Crystal structure of the peptidyl-cysteine decarboxylase EpiD complexed with a pentapeptide substrate. EMBO J. *19*, 6299–6310.

Bowers, W.F., Czubaroff, V.B., and Haschemeyer, R.H. (1970). Subunit structure of L-aspartate beta-decarboxylase from *Alcaligenes faecalis*. Biochemistry *9*, 2620–2625.

Brunger, A.T. (1993). Assessment of phase accuracy by cross validation: the free R value. Methods and applications. Acta Crystallogr. D. Biol. Crystallogr. *49*, 24–36.

Brunger, A.T., Adams, P.D., Clore, G.M., DeLano, W.L., Gros, P., Grosse-Kunstleve, R.W., Jiang, J.S., Kuszewski, J., Nilges, M., Pannu, N.S., et al. (1998). Crystallography and NMR system: a new software suite for macromolecular structure determination. Acta Crystallogr. D. Biol. Crystallogr. *54*, 905–921.

Brzovic, P., Holbrook, E.L., Greene, R.C., and Dunn, M.F. (1990). Reaction mechanism of *Escherichia coli* cystathionine γ-synthase: direct evidence for a pyridoxamine derivative of vinylglyoxylate as a key intermediate in pyridoxal phosphate dependent γ-elimination and γ-replacement reactions. Biochemistry *29*, 442–451.

Chang, C.C., Laghai, A., O'Leary, M.H., and Floss, H.G. (1982). Some stereochemical features of aspartate beta-decarboxylase. J. Biol. Chem. *257*, 3564–3569.

Chen, C.C., Chou, T.L., and Lee, C.Y. (2000). Cloning, expression and characterization of L-aspartate β-decarboxylase gene from *Alcaligenes faecalis* CCRC11585. J. Ind. Microbiol. Biotechnol. *25*, 132–140.

Chibata, I., Kakimoto, T., and Kato, J. (1965). Enzymatic production of L-alanine by *Pseudomonas dacunhae*. Appl. Microbiol. *13*, 638–645.

Chibata, I., Kakimoto, T., Kato, J., Shibatani, T., and Nishimura, N. (1967). Crystalline aspartic beta-decarboxylase of *Pseudomonas dacunhae*. Biochem. Biophys. Res. Commun. *26*, 662–667.

Domingo, G.J., Orru', S., and Perham, R.N. (2001). Multiple display of peptides and proteins on a macromolecular scaffold derived from a multienzyme complex. J. Mol. Biol. *305*, 259–267.

Dunathan, H.C. (1966). Conformation and reaction specificity in pyridoxal phosphate enzymes. Proc. Natl. Acad. Sci. USA *55*, 712–716.

Edwards, P.M. (2002). Origin 7.0: scientific graphing and data analysis software. J. Chem. Inf. Comput. Sci. *42*, 1270–1271.

Eliot, A.C., and Kirsch, J.F. (2004). Pyridoxal phosphate enzymes: mechanistic, structural, and evolutionary considerations. Annu. Rev. Biochem. *73*, 383–415.

Graber, R., Kasper, P., Malashkevich, V.N., Strop, P., Gehring, H., Jansonius, J.N., and Christen, P. (1999). Conversion of aspartate aminotransferase into an L-aspartate beta-decarboxylase by a triple active-site mutation. J. Biol. Chem. *274*, 31203–31208.

Grant, R.A., Filman, D.J., Finkel, S.E., Kolter, R., and Hogle, J.M. (1998). The crystal structure of Dps, a ferritin homolog that binds and protects DNA. Nat. Struct. Biol. *5*, 294–303.

Holm, L., and Sander, C. (1996). Mapping the protein universe. Science *273*, 595–603.

Jansonius, J.N. (1998). Structure, evolution and action of vitamin B6-dependent enzymes. Curr. Opin. Struct. Biol. *8*, 759–769.

Jones, T.A., Zou, J.Y., Cowan, S.W., and Kjeldgaard, M. (1991). Improved methods for building protein models in electron density maps and the location of errors in these models. Acta Crystallogr. A *47*, 110–119.

Kraulis, P.J. (1991). MOLSCRIPT: a program to produce both detailed and schematic plots of protein structure. J. Appl. Cryst. *24*, 946–950.

Krupka, H.I., Huber, R., Holt, S.C., and Clausen, T. (2000). Crystal structure of cystalysin from *Treponema denticola*: a pyridoxal 5′-phosphate-dependent protein acting as a haemolytic enzyme. EMBO J. *19*, 3168–3178.

Laskowski, R.A., MacArthur, M.W., Moss, D.S., and Thornton, J.M. (1993). PROCHECK: a program to check the stereochemical quality of protein structures. J. Appl. Cryst. *26*, 283–291.

Lee, H.S., Kim, M.S., Cho, H.S., Kim, J.I., Kim, T.J., Choi, J.H., Park, C., Lee, H.S., Oh, B.H., and Park, K.H. (2002). Cyclomaltodextrinase, neopullulanase, and maltogenic amylase are nearly indistinguishable from each other. J. Biol. Chem. *277*, 21891–21897.

McPhalen, C.A., Vincent, M.G., and Jansonius, J.N. (1992). X-ray structure refinement and comparison of three forms of mitochondrial aspartate aminotransferase. J. Mol. Biol. *225*, 495–517.

Meister, A., Sober, H.A., and Tice, S.V. (1951). Enzymatic decarboxylation of aspartic acid to alpha-alanine. J. Biol. Chem. *189*, 577–590.

Merritt, E.A., and Murphy, M.E.P. (1994). Raster3D version 2.0: a program for photorealistic molecular graphics. Acta Crystallogr. D. Biol. Crystallogr. *50*, 869–873.

Novogrodsky, A., Nishimura, J.S., and Meister, A. (1963). Transamination and beta-decarboxylation of aspartate catalyzed by the same pyridoxal phosphate-enzyme. J. Biol. Chem. *238*, 1903–1905.

Otwinowski, Z., and Minor, W. (1997). Processing of x-ray diffraction data collected in oscillation mode. Methods Enzymol. *276*, 307–326.

Rosenberg, R.M., and O'Leary, M.H. (1985). Aspartate beta-decarboxylase from *Alcaligenes faecalis*: carbon-13 kinetic isotope effect and deuterium exchange experiments. Biochemistry *24*, 1598–1603.

Rozzell, J.D. (1991). Method and compositions for the production of L-alanine and derivatives thereof. US Patent No. 5019509.

Russo, S., and Baumann, U. (2004). Crystal structure of a dodecameric tetrahedral-shaped aminopeptidase. J. Biol. Chem. *279*, 51275–51281.

Schoehn, G., Vellieux, F.M., Asunción Durá, M., Receveur-Bréchot, V., Fabry, C.M., Ruigrok, R.W., Ebel, C., Roussel, A., and Franzetti, B. (2006). An archaeal peptidase assembles into two different quaternary structures: A tetrahedron and a giant octahedron. J. Biol. Chem. *281*, 36327–36337.

Soda, K., Novogrodsky, A., and Meister, A. (1964). Enzymatic desulfination of cysteine sulfinic acid. Biochemistry *3*, 1450–1454.

Tate, S.S., and Meister, A. (1969). Regulation of the activity of L-aspartate beta-decarboxylase by a novel allosteric mechanism. Biochemistry *8*, 1660–1668.

Tate, S.S., and Meister, A. (1970). Regulation and subunit structure of aspartate beta-decarboxylase. Studies on the enzymes from *Alcaligenes faecalis* and *Pseudomonas dacunhae*. Biochemistry *9*, 2626–2632.

Tate, S.S., and Meister, A. (1971). L-aspartate-beta-decarboxylase: structure, catalytic activities, and allosteric regulation. Adv. Enzymol. Relat. Areas Mol. Biol. *35*, 503–543.

Terwilliger, T.C. (2000). Maximum likelihood density modification. Acta Crystallogr. D. Biol. Crystallogr. *56*, 965–972.

Terwilliger, T.C. (2002). Automated main-chain model-building by template-matching and iterative fragment extension. Acta Crystallogr. D. Biol. Crystallogr. *59*, 33–44.

Terwilliger, T.C., and Berendzen, J. (1999). Automated MAD and MIR structure solution. Acta Crystallogr. D. Biol. Crystallogr. *55*, 849–861.

Toney, M.D., and Krisch, J.F. (1993). Lysine 258 in aspartate aminotransferase: Enforcer of the Circe effect for amino acid substrates and the general-base catalyst for the 1,3-prototropic shift. Biochemistry *32*, 1471–1479.

Villeret, V., Tricot, C., Stalon, V., and Dideberg, O. (1995). Crystal structure of *Pseudomonas aeruginosa* catabolic ornithine transcarbamoylase at 3.0-Å resolution: a different oligomeric organization in the transcarbamoylase family. Proc. Natl. Acad. Sci. USA *92*, 10762–10766.

Wang, N.C., and Lee, C.Y. (2006). Molecular cloning of the aspartate 4-decarboxylase gene from *Pseudomonas* sp. ATCC 19121 and characterization of the bifunctional recombinant enzyme. Appl. Microbiol. Biotechnol. *73*, 339–348.

Wang, N.C., and Lee, C.Y. (2007). Enhanced transaminase activity of a bifunctional L-aspartate 4-decarboxylase. Biochem. Biophys. Res. Commun. *356*, 368–373.

Wang, N.C., Ko, T.P., and Lee, C.Y. (2008). Inactive S298R disassembles the dodecameric L-aspartate 4-decarboxylase into dimers. Biochem. Biophys. Res. Commun. *374*, 134–137.

Wilson, E.M., and Kornberg, H.L. (1963). Properties of crystalline L-aspartate 4-carboxy-lyase from *Achromobacter* sp. Biochem. J. *88*, 578–587.

